



# Fabrication of compressible and recyclable macroscopic $\text{g-C}_3\text{N}_4/\text{GO}$ aerogel hybrids for visible-light harvesting: A promising strategy for water remediation

Liang Tang <sup>a,\*</sup>, Cheng-ao Jia <sup>a</sup>, Yuan-cheng Xue <sup>a</sup>, Lin Li <sup>a</sup>, An-qi Wang <sup>a</sup>, Gang Xu <sup>a</sup>, Ning Liu <sup>b</sup>, Ming-hong Wu <sup>a,\*</sup>

<sup>a</sup> Shanghai Institute of Applied Radiation, School of Environmental and Chemical Engineering, Shanghai University, Shanghai 200444, PR China

<sup>b</sup> School of Environment and Architecture, University of Shanghai for Science and Technology, Shanghai 200093, PR China



## ARTICLE INFO

### Article history:

Received 8 February 2017

Received in revised form 12 July 2017

Accepted 19 July 2017

Available online 22 July 2017

### Keywords:

Graphitic carbon nitride ( $\text{g-C}_3\text{N}_4$ )

Three dimensional graphene oxide aerogel (3D GOA)

$\pi$ - $\pi$  Stacking interaction

Photoreduction

Superoxide radical anion

## ABSTRACT

Herein, a  $\text{g-C}_3\text{N}_4/\text{GO}$  aerogel hybrid with macroscopic 3D architecture is fabricated and applied in visible-light-induced water mediation. The composite photocatalyst with compressibility and recyclability is extraordinarily suitable for practical application. The morphologies and properties are carefully characterized, suggesting  $\text{g-C}_3\text{N}_4$  is well decorated on the surface of GO by  $\pi$ - $\pi$  stacking and the GO sheets are well interlaced. A moderate amount of  $\text{g-C}_3\text{N}_4$  in the hybrid is beneficial to photocatalytic activity for dyes and bromates. When the mass ratio of  $\text{g-C}_3\text{N}_4$  and GO is 3:5, the % degradation of MO and MB ( $20 \text{ mg L}^{-1}$ ) can reach ~90% in 40 min visible-light illumination, and % conversion of bromate ( $250 \text{ }\mu\text{g L}^{-1}$ ) can be obtained almost 80% in 60 min illumination. Underlying premise of maintaining intact macro appearance, the photocatalytic performance of the hybrid scarcely any lowers after 5 successive runs on degradation of MO, and the mass loss is below 4%. The composite mainly interacts with the contaminants by  $\pi$ - $\pi$  adsorption, implying it can be an important broad-spectrum photocatalyst since most of the contaminants in the environments contain  $\pi$ -bond structure. Through scavenger experiments and ESR determination, peroxide radical anions are proven as the predominant species during the photodegradation processes.

© 2017 Elsevier B.V. All rights reserved.

## 1. Introduction

The issues of energy shortage and environmental pollution are the hottest topics around the world, no matter in research communities and common population. However, energy development and environmental protection always occurred as some kind of paradox in the last century [1,2]. Recently, with the rapid development of novel functional materials, harvesting energy from the inexhaustible solar becomes more and more practicable [3,4]; moreover, applications of the solar for water remediation have attracted increasing interests [5,6]. As stated by the previous researches, nanomaterials with the properties of semiconductors including plasma [7], metal oxides/sulfides [8,9], metal-organic frames (MOFs) [10] and non-metallic materials [11] have shown excellent functions of environmental remediation.

Graphitic carbon nitride ( $\text{g-C}_3\text{N}_4$ , CN), a new generation of metal-free material with a band gap of ~2.7 eV exhibiting distinct electronic structure and chemical properties, has been successfully tested in energy conversion and storage, [12] electro-/photocatalysis, [13,14] supercapacitors [15] and sensors [16]. However, practically achieving sustainability with the photocatalysts in the environment still has a long way to go; since some drawbacks like micro-scale of materials restricting recycling operation and recombination of photon-generated carriers extremely impede the practical applications of pristine CN. In addition, most of CN existing in the form of polymers with low crystallinity limits the efficiency associated to high excitation dissociation energy and charge mobility [17]. If the nanomaterials are ever to be utilized as components of practical, macroscopic devices on a large scale, there is also a complementary need to construct the materials into more sophisticated, hierarchical and macroscopic three-dimensional (3D) architectures [18].

3D graphene oxide aerogels (GOAs) with macroscopic block appearance are considered as an ideal photocatalytic candidate, which could be conveniently recycled from the water and provide support for the deposition photocatalysts [19–21]. Furthermore,

\* Corresponding authors.

E-mail addresses: [tang1liang@shu.edu.cn](mailto:tang1liang@shu.edu.cn) (L. Tang), [\(M.-h. Wu\).](mailto:mhwu@shu.edu.cn)

exceptional high surface area and excellent electrical conductivity make GOAs good photocatalytic reaction site [22,23]. Whereas, it is a pity that if the photocatalysts were not anchoring on the supports, they would leach into water, and lead to reducing photocatalytic performance and nanoparticle pollution. Due to the internally connected conductive network structure and special internal microenvironment of GOAs, they are also widely used in energy storage [24], catalyst [25], environmental protection [26], retractable conductors and other fields [27,28]. In addition, the shape, volume and density of the 3D GOAs can be easily controlled by modulation of the reaction vessel characteristics compared to 2D graphene, indicating the possibility and feasibility of large-scale production [29].

Herein, we chemically exfoliated bulk CN (BCN) to exfoliated CN sheets, and then fabricated the CN sheets on surface of GOA to form macroscopic hybrid architecture. The application of metal-free catalysts can avoid the anxiousness about potential ecotoxicity induced by metallic nanocatalysts [30,31]. CN nanocrystalline sheets show stable chemical structure and high photo-quantum efficiency. The  $\pi$ - $\pi$  stacking and hydrogen-bonding interactions between CN and graphene oxide (GO) supply photo-excited electrons favorable transferring channels [32], and leads to beneficial separation of photo-generated carriers; meanwhile, conjugated adsorption and curly encapsulation by GO sheet make CN stable incorporation with GOA support. Owing to the ultra-light weight, the hybrid photocatalyst can float on the top surface of target water medium, and easily absorb the above light. In the present study, photocatalytic oxidation aiming to two kinds of dyes, methyl orange (MO) and methylene blue (MB) representing anionic and cationic dyes, and reduction of carcinogenic bromate are both conducted via the novel hybrids to test the general water remediation possibilities.

## 2. Experimental details

### 2.1. Preparation of the GO and CN

GO was prepared by oxidation of the natural graphite powder using a modified Hummers method reported elsewhere [33]. The CN samples were prepared as follows: firstly, 10 g dicyandiamide powder was heated at 550 °C for 4 h. After cooling to room temperature, yellow bulk CN was obtained. Then, 5 g bulk CN was further treated by 100 mL sulphuric acid ( $H_2SO_4$ ) with vigorous stirring for 20 h. Whereafter, 1 g sodium nitrate ( $NaNO_3$ ) and 10 g potassium permanganate ( $KMnO_4$ ) were slowly added into the CN solution under the condition of ice bath and stirred for 10 h under ambient condition. Then, the mixture solution was diluted to 300 mL with deionized water (140 mL) and 30% hydrogen peroxide (60 mL) under the condition of ice bath. Finally, the white product solution was obtained by dialyzing the diluted solution for 3 days, then suction filtration and drying at 55 °C for 24 h. The general fabrication procedure of CN/GOA hybrid is briefly illustrated in [Scheme 1](#).

### 2.2. Synthesis of CN/GO aerogels

An amount of 2 mL CN suspensions was mixed with 3 mL of GO (5 mg mL<sup>-1</sup>) aqueous solution with mass ratio of 3:5 of CN to GO under ultrasonication for 30 min. After that, ethylenediamine (80  $\mu$ L) was added into mixture and the mixture was sealed in a glass vessel and heated at 95 °C, and then a certain amount of cetyltrimethyl ammonium bromide (CTAB) was added into mixture and the mixture was heated for 7 h at 95 °C for synthesis of functionalized graphene hydrogel. After freeze-drying for 48 h, the solvent within the hydrogel was completely removed and the functionalized graphene aerogel (CN/GOA) was produced. A series of

CN/GOA photocatalysts were prepared by varying the mass ratio of CN to GO ( $m_{GO}:m_{-C_3N_4} = 10.00, 5.00, 2.50, 1.67$  and 1.25), which are denoted as 1.5-CN/GOA, 3-CN/GOA, 6-CN/GOA, 9-CN/GOA and 12-CN/GOA, respectively.

### 2.3. Characterization of CN/GO aerogels

Transmission electron microscope (TEM) and high resolution transmission electron microscopy (HRTEM) observations were performed on a JEOL JEM-2010F electron microscope operating at 200 kV. Scanning electronic microscopy (SEM) images were taken with Hitachi FESEM-4800. UV-vis absorption spectra were recorded at room temperature on a Hitachi 3100 spectrophotometer. X-ray diffraction (XRD) patterns were obtained with a Rigaku 18 KW D/max-2550 using Cu Ka radiation. Fourier transform infrared spectroscopy (FT-IR) was performed on Thermo Nicolet Avatar 370 FT-IR. X-Ray photoelectron spectrometer (XPS) was collected using a Kratos Axis Ultra DLD X-ray photoelectron spectrometer. Electron spin resonance (ESR) was detected using a JEOL JES-FA200 ESR. The surface properties were determined through BET (Brunauer-Emmett-Teller) analysis by a BET-201-AEL Sorptometer. High-purity N<sub>2</sub> was used as the adsorbent and the sample out gassed to 20 mm vacuum at 120 °C.

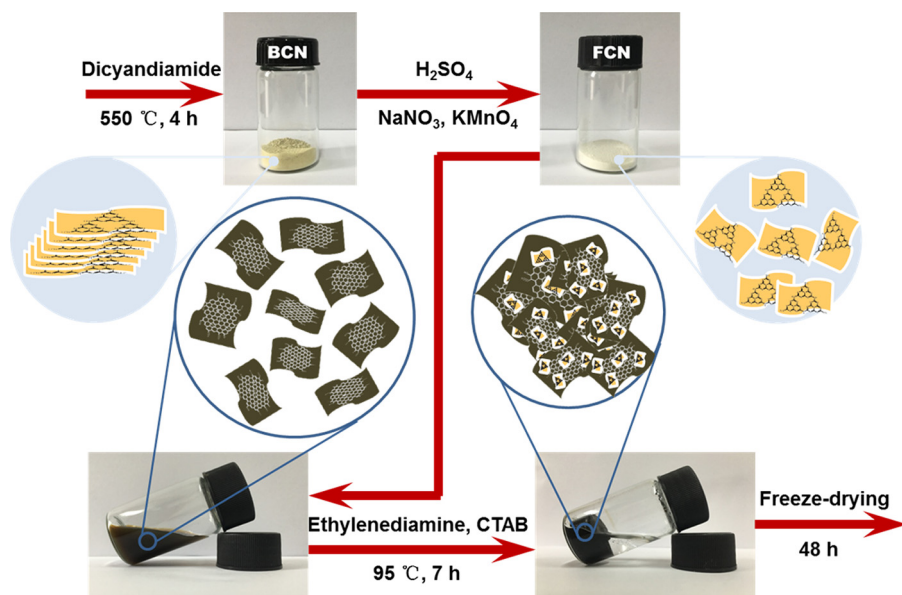
### 2.4. Photocatalytic performance

Photocatalytic activities of as-prepared CN/GOAs were evaluated by the degradation of methyl orange (MO, 20 mg L<sup>-1</sup>) in an aqueous solution under 300 W Xe lamp (Nanjing Sidongke Electrical Equipment Co., China) with a cut off filter ( $\lambda > 420$  nm). CN/GOA photocatalyst was participated in a 50 mL MO solution in a 60 mL quartz tube. Prior to illumination, the dye solution was magnetically stirred for 15 min in the dark to ensure that the hybrid surface was saturated with MO molecules. Every illumination interval, 1.0 mL suspension was sampled and analyzed with a UV-vis spectrophotometer at the maximal absorption wavelength of MO (465 nm). Accordingly, the photodegradation for methyl blue (MB, 20 mg L<sup>-1</sup>) and photoreduction for BrO<sub>3</sub><sup>-</sup> (250  $\mu$ g L<sup>-1</sup>) under visible-light illumination over the photocatalysts were also tested.

## 3. Results and discussion

### 3.1. Morphology and structure of the as-prepared hybrid

The digital photo of as-prepared composite shows a macroscopic scale ([Fig. 1a](#)), whose shape and size can be easily controlled by change of the synthesis container. What is more, the composite is relatively compressible, which can cope with in term of gravity (100g counterweight) and completely recover soon ([Fig. S1](#)). That is to say, the CN/GOA hybrid is mechanically robust and suitable for water remediation in those complicated hydrological conditions. The morphology of CN/GOA was first measured by scanning electron microscopy (SEM). As illustrated in [Fig. 1b](#), an interconnected, porous 3D GO architecture with continuous macropores in the micrometer size range was constructed. Transmission electron microscopy (TEM) characterization validates the CN sheets (with size of ~100 nm) uniformly distribute on the GO surface ([Fig. 1c](#)), it is noteworthy that some CN is layered stacked with GO, and other portion of CN is encapsulated within graphene layers, both suggesting CN sheets are well assembly with GO sheets. High-resolution TEM (HRTEM) reveals typical CN sheet with as well crystalline texture stack on the surface of GO, or is encapsulated by GO sheet ([Fig. 1d,e](#)). Remarkably, CN on GO film is formed in clear crystalline phase rather than amorphous form, and the lattice distance is measured as 0.324 nm, which is ascribed to the interlayer stacking of aromatic segments of CN [34,35]. The crystalline CN



**Scheme 1.** Schematic diagram of the fabrication route for the CN/GOA hybrid.

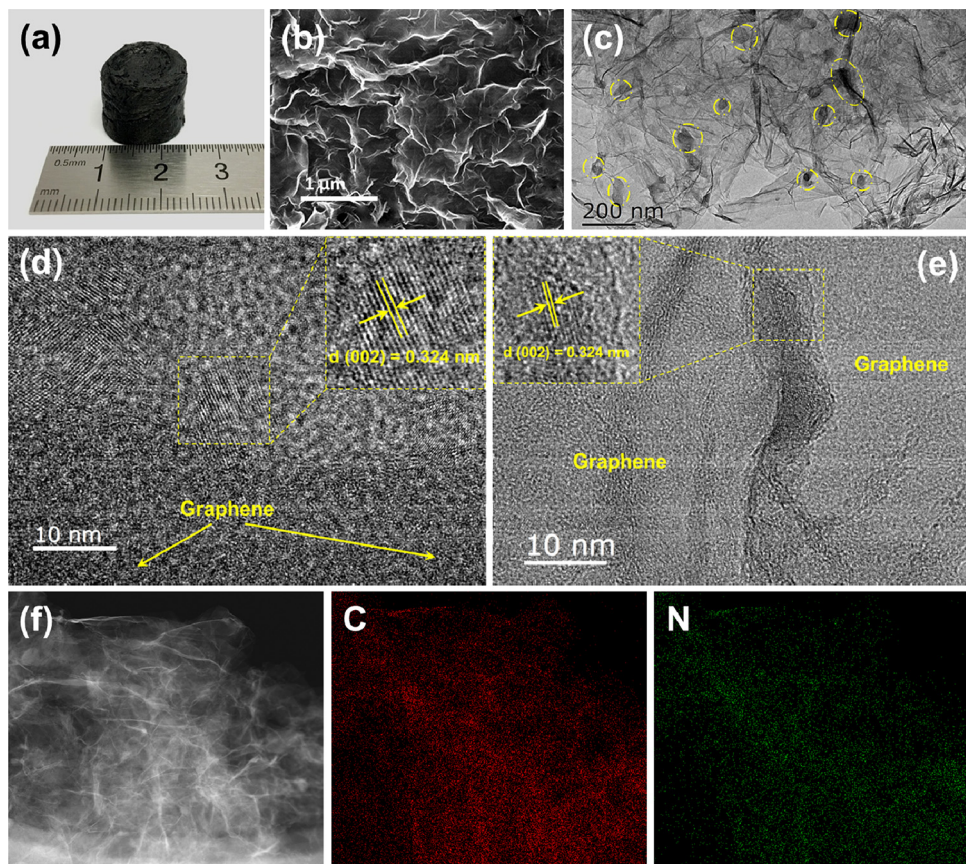


**Fig. 1.** (a) Digital image of the as-prepared CN/GOA hybrid, (b) SEM image, (c–e) high-magnification TEM images and HRTEM images, and (f) HAADF image and the corresponding C and N elemental mapping of CN/GOA hybrid.

exhibits graphitic structure, high thermal and chemical stability, as well as semiconductor electronic structure [36], which can support the catalytic reactions processing stably. Scanning TEM (STEM) and elemental mapping analysis of CN/GOA composite suggest the presence and distribution of C and N components in the as-prepared catalyst (Fig. 1f). It is notable that N element is uniformly distributed on C basement, which is also verified by energy dispersive X-ray

spectroscopy (EDS) line scanning (Fig. S2), further evidencing CN nanosheets well decorate GO.

The crystal structure and phase composition of CN, GOA and as-prepared hybrids were characterized by XRD X-ray diffraction (XRD) (Fig. 2a). XRD patterns reveal that two distinct diffraction peaks appear at  $27.4^\circ$  and  $12.8^\circ$  in BCN; the intensive peak corresponds to the characteristic (002) plane interlayer stacking, while

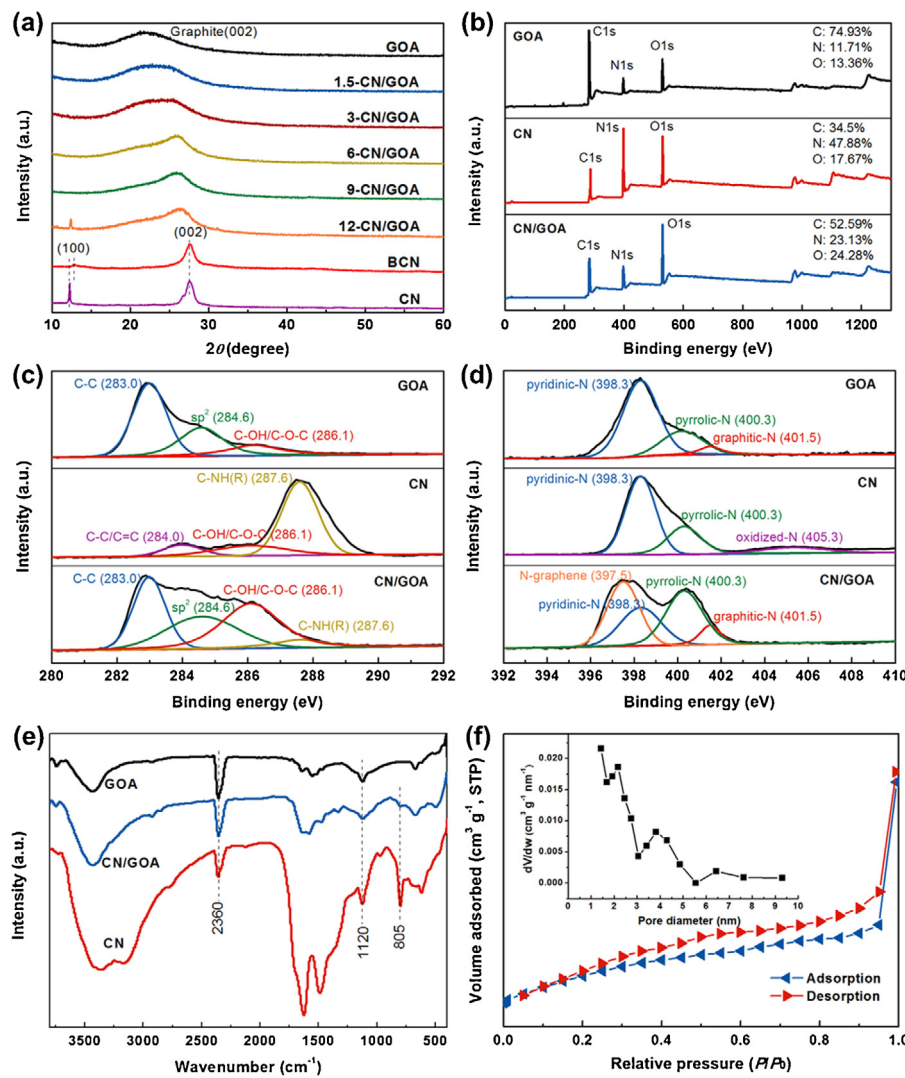


**Fig. 2.** (a) XRD patterns of the prepared photocatalysts, (b–d) XPS spectra and (e) FTIR spectra of pristine CN, GO and CN/GOA hybrid, (f) nitrogen adsorption-desorption isotherm and the corresponding pore diameter distribution curve of CN/GOA hybrid.

the weak one (100) is attributed to an in-planar repeat period, such as the distance between the nitrogen pores [37]. Compared with XRD pattern of BCN, the peak of  $27.6^\circ$  becomes sharper after exfoliation and protonation, indicating exfoliated CN has a higher crystallinity than BCN. It is noted that the stacking distance of 0.324 nm from the interlayer-stacking of the conjugated aromatic system corresponding to (002) plane is in agreement with the lattice distance of CN observed by HRTEM (Fig. 1d,e). Besides, the peak of (100) plane is observed shifting from  $12.8^\circ$  to  $12.3^\circ$  and becomes intensive sharp, suggesting the regular in-planar connection of tri-s-triazine units in the CN layers is appeared [38]. On the other hand, a broad diffraction peak at around  $22.6^\circ$  is observed for the GOA, suggesting that the GO sheets are loosely stacked [39]. This can be ascribed to the bridge-link between the GO sheets by amine released from ethanediamine [40]; and the bridge-link can significantly enhance the mechanical strength of the 3D architecture. With the increase content of CN in CN/GOA hybrids, the diffraction peak gradually shifts toward a higher angle to  $26.3^\circ$ , and no diffraction peak related to the CN homogeneous phase is occurred, indicating an interaction between crystalline CN and GO occurs, and CN sheets are well separated by GO sheets in CN/GOA hybrids [41,42].

The characterization of elemental composition as well as functional groups of CN/GOA hybrid was further determined by X-ray photoelectron spectroscopy (XPS) (Fig. 2b–d). The overall XPS spectra from Fig. 2b suggest C, N and O elements as dominant elemental components exist in GOA, CN and CN/GOA hybrid. Fig. 2c illustrated a deconvoluted XPS C1s spectrum of samples. There are four distinct peaks occur at 283.0, 284.6, 286.1 and 287.6 eV, corresponding to C–C,  $sp^2$  C=C, C–OH/C–O–C and C–NH(R) bonds, respectively [40,43,44]. Obviously, the functional groups in composite are mainly constituted from those of GOA and CN, implying CN sheets are well incorporated with GOA. Whereas, the 284.0 eV peak originating from  $sp^2$ -bonded carbon network (C–C/C=C) in pristine CN disappear in the spectrum of CN/GOA [45], which is an evidence that in-planar connection of CN is destroyed after the intercalation of GO sheets. A deconvoluted N1s spectrum of CN/GOA hybrid is shown in Fig. 2d, which presents four types of N species including 33.2% N-graphene (397.5 eV), 24.8% pyridinic-N (398.3 eV), 34.2% pyrrolic-N (400.3 eV), 7.8% graphitic-N (401.5 eV), respectively [46]. Expectedly, pyridinic-N, pyrrolic-N and graphitic-N in CN/GOA hybrid are the main components from pristine GOA and CN; while the distinct peak of N-graphene appeared in the hybrid can be attributed to the formation of C–N–C bonding, which can be served to link CN with GOA forming stable incorporation [47].

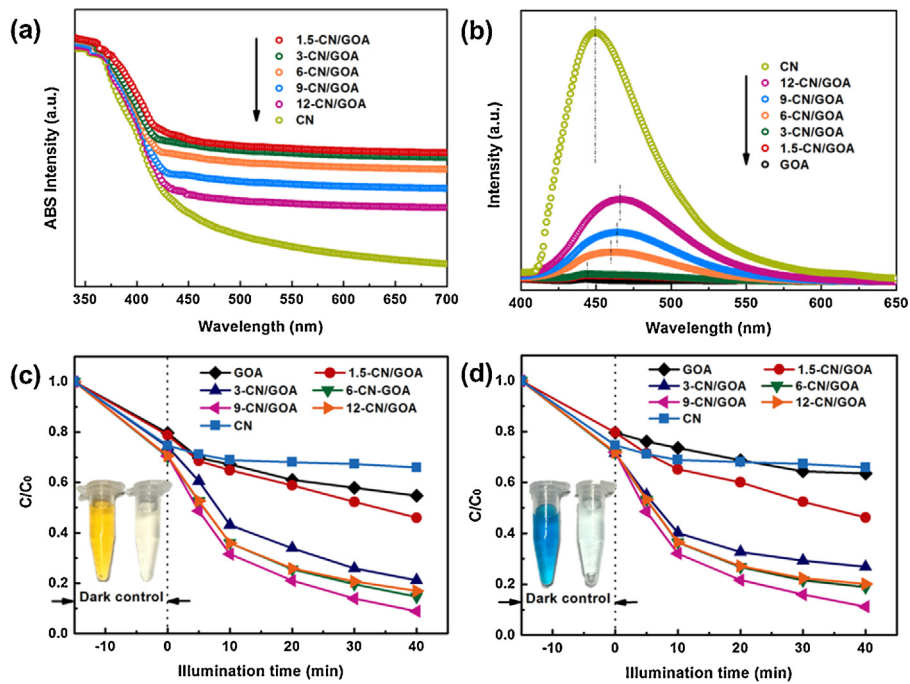


**Fig. 3.** Optical properties of CN, GOA and CN/GOA hybrids measured by (a) UV-vis DRS and (b) PL, and their visible-light catalytic performance on (c) anionic dye MO and (d) cationic dye MB. Inserted photos: (c) MO and (d) MB solutions before and after 40 min illumination over 9-CN/GOA photocatalyst.

Fourier transform infrared (FTIR) spectrum displays typical stretching modes of CN heterocycles ( $1200\text{--}1650\text{ cm}^{-1}$ ) and the breathing mode of triazine units ( $805\text{ cm}^{-1}$ ) (Fig. 2e) [48]. Those CN-like peaks can also be found in CN/GOA hybrid, however, the signals are covered and weak due to the low content of CN in the hybrid. A broad peak at  $3300\text{--}3500\text{ cm}^{-1}$  from the stretching mode of  $-\text{OH}$  could be vaguely related to GO in CN/GOA as previous report [49]. The presence of the  $\text{C}-\text{O}-\text{C}$  groups in the hybrid is indicated by the peak at an antisymmetric stretching of  $1120\text{ cm}^{-1}$  [50]. Besides, the band appearing at  $2360\text{ cm}^{-1}$  relating to the stretching vibration of gas phase  $\text{CO}_2$  is routinely observed in the background scan on an FTIR measurement in the air atmosphere [51].

The  $\text{N}_2$  adsorption-desorption suggests the BET (Brunauer-Emmett-Teller) surface and porous structures of the as-prepared CN/GOA hybrid (Fig. 2f). The adsorption-desorption isotherm is identified as type IV with an H3 hysteresis loop according to the IUPAC classification [52]. This information elucidates the presence of mesoporous structure and slit-like pores in CN/GOA hybrid. Furthermore, the pore size distribution relating to measurement can be plotted by the BJH (Barret-Joyner-Halenda) method, which is inserted in Fig. 2f. The pore size distribution plot shows that the hybrid exhibits a narrow distribution in the range of  $2\text{--}5\text{ nm}$ , which is possibly ascribed to the interlaced assemblies of GO nanosheets.

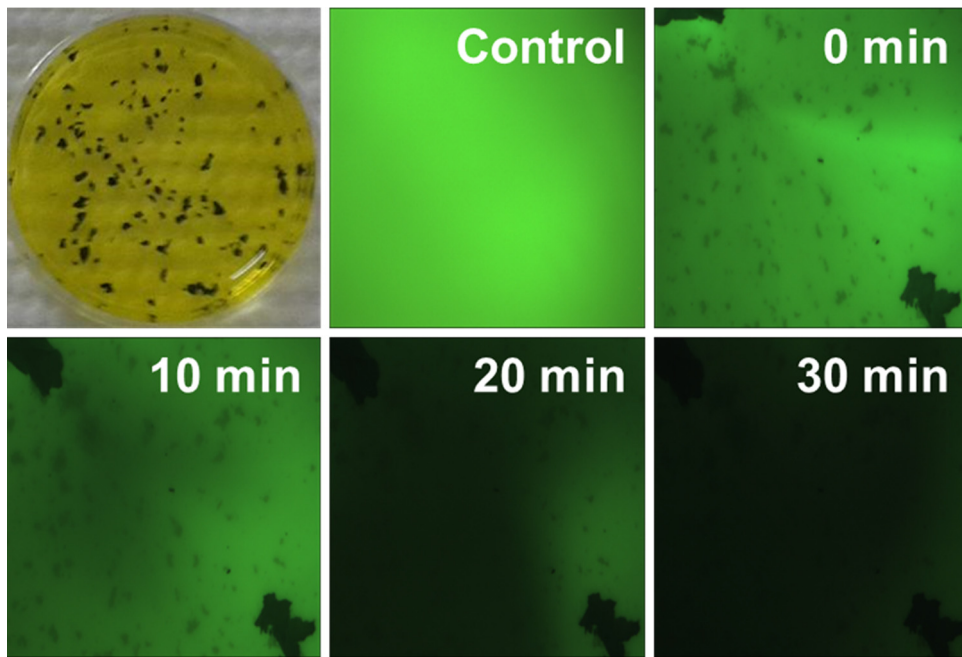
### 3.2. Optical properties of the hybrid

Fig. 3a depicts the UV-vis diffuse reflectance spectra (DRS) of the pristine CN, GOA, and CN/GOA architectures. As shown, all investigated samples exhibit strong visible-light absorption. Obviously, with the incorporation of GOA, the hybrids show similar absorption edge as compared with pristine CN at  $\sim 430\text{ nm}$ , demonstrating intrinsic band gap of CN/GOA is mainly originated from the electron transitions from the valence band (VB) to the conduction band (CB) of CN [53]. The incorporation of GOA dose not reduce the light absorption ability of CN; contrarily, the  $E_g$  value of CN/GOA hybrid ( $2.65\text{ eV}$ ) is slightly lower than that of pristine CN ( $2.71\text{ eV}$ ) (Fig. S3), meaning the hybrid can more effectively absorb visible light. Fig. 3b

illustrates the PL spectra of the as-prepared composites as well as pristine CN and GOA, which can supply the information about separation efficiencies of the photo-induced electron-hole ( $e^- - h^+$ ) pairs in those materials. It is evidenced that combination of CN with GOA can harshly reduce the PL intensity, revealing the recombination of  $e^- - h^+$  pairs transferred on CN surface is impeded. It is well understandable, since the photo-excited electrons can be rapidly transferred via the 3D graphene network, and reducing the probability of recombination. Moreover, significant red-shifts in the PL spectra are observed after incorporation with GOA, which may be relating to molecular conjugation between CN and GO [54]. It can be also found that the PL signals exhibit gradual shift to longer wavelength with increase content of CN in the hybrids. Thus it can be seen the as-prepared hybrid not only enhances the light-absorption properties, but can also inhibit the recombination of photo-induced carriers, making this hybrid a good photocatalytic candidate.

### 3.3. Visible-light driven catalytic performance

To evaluate the potential application of CN/GOA in water remediation, MO and MB were used as the target model contaminants to study the visible-light catalytic performance of the as-synthesized hybrid. Fig. 3c,d display the degradation curves representing visible-light catalytic efficiencies for MO and MB by CN, GOA and CN/GOA with distinct CN contents, respectively. Within 40 min visible-light illumination after 15 min adsorption equilibrium, pristine CN and GOA show the lowest degradation efficiencies for both MO and MB among all the materials. Aside from CN and GOA, the CN/GOA hybrids exhibit better photocatalytic performance than their parent counterparts. The degradation efficiency gradually increases with the increase of CN contents from  $1.5\text{ mg}$  to  $9\text{ mg}$ , suggesting sufficient CN crystalline sheets in hybrid can enhance the catalytic activities. Notably particularly, 9-CN/GOA reduces ca. 91.1% and 88.8% of MO and MB in 40 min visible-light illumination, and the degradation rate constants are calculated as  $0.0498$  and  $0.0443\text{ min}^{-1}$  for MO and MB, respectively (Figs. 3c,d and S4).



**Fig. 4.** Digital photo and fluorescence image of the adsorption on FITC, and the fluorescence images of FITC over the adsorption by 9-CN/GOA at 0, 10, 20 and 30 min, respectively.

The extremely high efficiencies aiming to both anionic and cationic dyes suggest the hybrid mainly adsorbs the contaminants based on the  $\pi$ - $\pi$  interaction [55], rather than ionic or electrostatic adsorption, which is also strongly supported by the adsorption tests on fluorescein isothiocyanate (FITC) (Fig. 4). It is observed that the hybrid exhibits an obvious adsorption effect on FITC in 30 min. The fluorescence images at 10-min interval times were observed in the same location with the same conditions. With the increasing of adsorption time, the brightness of the fluorescence was significantly decreased in solution. It can be inferred that the fast fluorescence quenching of FITC is driven by adsorption of 9-CN/GOA through  $\pi$ - $\pi$  interactions. Consequently, the application for the hybrid in water remediation is expected to be highly effective and broad-spectrum.

Nevertheless, further lifting CN content to 12 mg in CN/GOA hybrid decreases the degradation efficiencies (the curves expressing 12-CN/GOA in Fig. 3c,d). The phenomena are attributed to extra CN in the hybrid. The excess CN may occupy the active sites for photocatalytic reactions on GO sheets, and lead to recombination of  $e^-$ - $h^+$  pairs taking place more possibly. In addition, the stability of the composite was tested by 5 degradation cycle runs. The curves suggest the degradation stability of MO with 9-CN/GOA is fantastically consistent (Fig. 5). The removal rate of MO can still reach 91.1% at 5th run within 40 min. Surprisingly, the weight loss of the catalyst is only 3.95% after 5 successive cycles (Fig. S5), verifying the reliability of the mechanical strength and repeating utilization. The comparisons of CN/GOA with representative  $\text{g-C}_3\text{N}_4$ -based photocatalysts reported elsewhere on the degradation of dye contaminants are summarized in Table S1.

Apart from the capacity of photodegradation, the as-prepared hybrids also exhibit the photoreduction ability. It has been proven that the composites can reduce the bromate content in solutions (Fig. S6); that is to say, the hybrids are expected to be used in dehalogenation of halogenated organic compounds and reduction treatment for Cr(VI), as well as other toxic substances with high oxidation states, and thus show broad-spectrum water-remediation capacities.

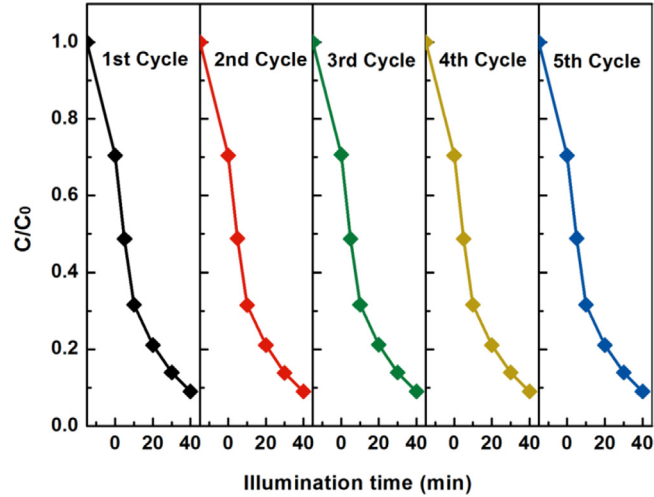


**Fig. 5.** Photocatalytic stability of 9-CN/GOA for MO within 5 cycle runs. The relative standard deviation (RSD) of  $C/C_0$  after 40 min irradiation of 5 runs is calculated as  $9.54 \times 10^{-5}$ .

### 3.4. Proposed photocatalytic mechanisms

Although we obtained fascinating water remediation performance by 9-CN/GOA hybrid, the radical scavenging experiments were carried out to further study the photocatalysis mechanisms as well. Herein, EDTA-2Na, isopropanol and *p*-benzoquinone were employed as the trappers for  $h^+$ ,  $\cdot\text{OH}$  and  $\text{O}_2^{\cdot-}$ , respectively [56]. Significantly, the degradation of MO is restrained in the presence of *p*-benzoquinone; however, EDTA-2Na and isopropanol play ignorable inhibition on MO degradation (Fig. 6a, the relevant degradation rate constants are depicted in Fig. S7). Interestingly, scavenging unpaired  $h^+$  by EDTA-2Na further enhances the degradation efficiency. All the phenomena suggest MO degradation depends on  $\text{O}_2^{\cdot-}$  greatly rather than  $\cdot\text{OH}$  and  $h^+$ . Scavenging unpaired  $h^+$  can reduce their recombination probability with  $e^-$ , hence  $\text{O}_2^{\cdot-}$  concentration may increase with the existence of EDTA-2Na in

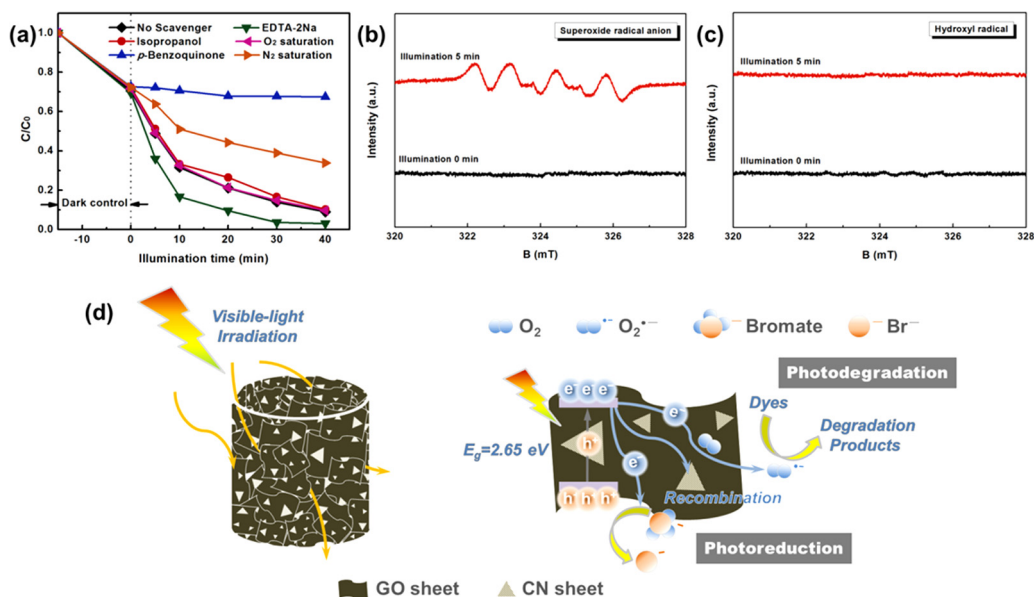


**Fig. 6.** (a) Effects of different scavengers on the MO degradation with 9-CN/GOA, ESR spectra of (b) DMPO-O<sub>2</sub><sup>•</sup>- and (c) DMPO-OH adducts, (d) schematic diagram of mechanisms for water remediation processes over the hybrid under visible-light irradiation.

aqueous solution, and leading to enhancement of degradation rate. The effect on MO degradation by trapping •OH can be negligible. According to previous studies, the top of the VB position of CN is located at about +1.40 V (vs. NHE, pH=7) [57], and is hard to oxidizing OH<sup>-</sup> into •OH ( $E^{\ominus}_{\text{OH}^-/\cdot\text{OH}} = +1.99$  V vs. NHE, pH=7) [58]. The effect of O<sub>2</sub><sup>•-</sup> was also confirmed through O<sub>2</sub> and N<sub>2</sub> saturation experiments. Fig. 6a illustrates MO degradation curve after exclusion of O<sub>2</sub> by injection of N<sub>2</sub>. As expected, the degradation efficiency with N<sub>2</sub> saturation is harshly lowered comparing with no scavenger participation and O<sub>2</sub> saturation, since the formation of O<sub>2</sub><sup>•-</sup> is hindered without adequate O<sub>2</sub> (O<sub>2</sub> + e<sup>-</sup> → O<sub>2</sub><sup>•-</sup>).

To further verify the roles of the free radical species on the photocatalysis process over CN/GOA hybrid materials, the electron spin resonance (ESR) spin-trap technique are performed. Fig. 6b,c illustrate no signal is recorded for both O<sub>2</sub><sup>•-</sup> and •OH without light illumination, suggesting there is no O<sub>2</sub><sup>•-</sup> and •OH radicals generated in dark conditions. When the light is on, the characteristic signals of the DMPO-O<sub>2</sub><sup>•-</sup> could be observed, whereas the characteristic signals of the DMPO-•OH still cannot be recorded. As a consequence, it can be confirmed that the O<sub>2</sub><sup>•-</sup> radicals play the crucial role in the photodegradation process rather than •OH. Base on the understandings above, the visible-light driven photocatalytic mechanisms are proposed as shown in Fig. 6d.

#### 4. Conclusions

Herein, we fabricated a mechanically robust and conveniently recyclable 3D g-C<sub>3</sub>N<sub>4</sub>/GO aerogel (CN/GOA) with tunable architecture, which is good visible-light response. Such macroscopic structure is of benefit to applications in water remediation in natural environments. The protonated CN nanosheets show good crystalline phase, and exhibit high thermal and chemical stability. The interaction between CN and GO sheets is mainly conducted by π-π stacking and hydrogen-bonding interactions, leading to the formed hybrid is more structurally stable and abundant electron-transfer channels. Moreover, such structure is more stable comparing with those materials combining nanoparticle with GO. The visible-light induced photodegradation for MO and MB evidences the excellent performance over the as-prepared hybrid. Furthermore, such hybrid also exhibits photoreduction

capacity directing to bromate ions in this study. Excitingly, underlying premise of maintaining intact macro appearance, the photocatalytic performance of CN/GOA hybrid scarcely any lowers after 5 successive runs on degradation of MO. In summary, the as-constructed material is potentially suitable for practical applications in water remediation aiming to broad-spectrum contaminants.

#### Acknowledgements

The authors of this work gratefully appreciate the financial support provided by National Natural Science Foundation of China (Nos. 41573096, 41473108 and 41673093), Program for Changjiang Scholars and Innovative Research Team in University (No. IRT13078).

#### Appendix A. Supplementary data

Supplementary data associated with this article can be found, in the online version, at <http://dx.doi.org/10.1016/j.apcatb.2017.07.053>.

#### References

- [1] D. Berg, A. Kovats, Energy without pollution, *Science* 170 (1970) 17–18.
- [2] L. Shen, L. Liu, Energy development and environmental protection dual challenges for China, *Energy Environ.* 2 (1991).
- [3] G.D. Scholes, G.R. Fleming, A. Olaya-Castro, R. van Grondelle, Lessons from nature about solar light harvesting, *Nat. Chem.* 3 (2011) 763–774.
- [4] O. Lopez-Sanchez, E.A. Llado, V. Koman, A.F.I. Morral, A. Radenovic, A. Kis, Light generation and harvesting in a van der Waals Heterostructure, *ACS Nano* 8 (2014) 3042–3048.
- [5] H.L. Zhou, Y.Q. Qu, T. Zeid, X.F. Duan, Towards highly efficient photocatalysts using semiconductor nanoarchitectures, *Energy Environ. Sci.* 5 (2012) 6732–6743.
- [6] H.B. Zhang, T. Wang, J.J. Wang, H.M. Liu, T.D. Dao, M. Li, G.G. Liu, X.G. Meng, K. Chang, L. Shi, T. Nagao, J.H. Ye, Surface-plasmon-enhanced photodriven CO<sub>2</sub> reduction catalyzed by metal-organic-framework-derived iron nanoparticles encapsulated by ultrathin carbon layers, *Adv. Mater.* 28 (2016) 3703–3710.
- [7] E.C. Neyts, K. Ostrikov, M.K. Sunkara, A. Bogaerts, Plasma catalysis: synergistic effects at the nanoscale, *Chem. Rev.* 115 (2015) 13408–13446.
- [8] M.B. Gawande, A. Goswami, F.X. Felpin, T. Asefa, X.X. Huang, R. Silva, X.X. Zou, R. Zboril, R.S. Varma, Cu and Cu-based nanoparticles: synthesis and applications in review catalysis, *Chem. Rev.* 116 (2016) 3722–3811.

[9] B.T. Yonemoto, G.S. Hutchings, F. Jiao, A general synthetic approach for ordered mesoporous metal sulfides, *J. Am. Chem. Soc.* 136 (2014) 8895–8898.

[10] C.M. Doherty, D. Buso, A.J. Hill, S. Furukawa, S. Kitagawa, P. Falcaro, Using functional nano- and microparticles for the preparation of metal-organic framework composites with novel properties, *Acc. Chem. Res.* 47 (2014) 396–405.

[11] X.D. Zhuang, Y.Y. Mai, D.Q. Wu, F. Zhang, X.L. Feng, Two-dimensional soft nanomaterials: a fascinating world of materials, *Adv. Mater.* 27 (2015) 403–427.

[12] W.J. Ong, L.L. Tan, Y.H. Ng, S.T. Yong, S.P. Chai, Graphitic carbon nitride (g-C<sub>3</sub>N<sub>4</sub>)-based photocatalysts for artificial photosynthesis and environmental remediation: are we a step closer to achieving sustainability? *Chem. Rev.* 116 (2016) 7159–7329.

[13] G. Mamba, A.K. Mishra, Graphitic carbon nitride (g-C<sub>3</sub>N<sub>4</sub>) nanocomposites: a new and exciting generation of visible light driven photocatalysts for environmental pollution remediation, *Appl. Catal. B-Environ.* 198 (2016) 347–377.

[14] J.S. Xu, M. Antonietti, M. Shalom, Moving graphitic carbon nitride from electrocatalysis and photocatalysis to a potential electrode material for photoelectric devices, *Chem.-Asian J.* 11 (2016) 2499–2512.

[15] Y.B. Ding, Y.H. Tang, L.M. Yang, Y.X. Zeng, J.L. Yuan, T. Liu, S.Q. Zhang, C.B. Liu, S.L. Luo, Porous nitrogen-rich carbon materials from carbon self-repairing g-C<sub>3</sub>N<sub>4</sub> assembled with graphene for high-performance supercapacitor, *J. Mater. Chem. A* 4 (2016) 14307–14315.

[16] Y.L. Li, S.P. Zhang, Q.R. Zhang, G.F. Xu, H. Dai, Y.Y. Lin, Binding-induced internal-displacement of signal-on photoelectrochemical response: a glyphosate detection platform based on graphitic carbon nitride, *Sens. Actuator B-Chem.* 224 (2016) 798–804.

[17] J.S. Zhang, J.H. Sun, K. Maeda, K. Domen, P. Liu, M. Antonietti, X.Z. Fu, X.C. Wang, Sulfur-mediated synthesis of carbon nitride: band-gap engineering and improved functions for photocatalysis, *Energy Environ. Sci.* 4 (2011) 675–678.

[18] K. Shehzad, Y. Xu, C. Gao, X.F. Duan, Three-dimensional macro-structures of two-dimensional nanomaterials, *Chem. Soc. Rev.* 45 (2016) 5541–5588.

[19] Y.Y. Fan, W.G. Ma, D.X. Han, S.Y. Gan, X.D. Dong, L. Niu, Convenient recycling of 3D AgX/graphene aerogels (X=Br, Cl) for efficient photocatalytic degradation of water pollutants, *Adv. Mater.* 27 (2015) 3767–3773.

[20] C. Cui, S. Li, Y.W. Qiu, H.H. Hu, X.Y. Li, C.R. Li, J.K. Gao, W.H. Tang, Fast assembly of Ag<sub>3</sub>PO<sub>4</sub> nanoparticles within three-dimensional graphene aerogels for efficient photocatalytic oxygen evolution from water splitting under visible light, *Appl. Catal. B-Environ.* 200 (2017) 666–672.

[21] J.P. Zou, H.L. Liu, J.M. Luo, Q.J. Xing, H.M. Du, X.H. Jiang, X.B. Luo, S.L. Luo, S.L. Suib, Three-dimensional reduced graphene oxide coupled with Mn<sub>3</sub>O<sub>4</sub> for highly efficient removal of Sb(III) and Sb(V) from water, *ACS Appl. Mater. Interface* 8 (2016) 18140–18149.

[22] H. Wu, L.T. Drzal, Graphene nanoplatelet paper as a light-weight composite with excellent electrical and thermal conductivity and good gas barrier properties, *Carbon* 50 (2012) 1135–1145.

[23] G.Q. Chen, Y.X. Liu, F. Liu, X. Zhang, Fabrication of three-dimensional graphene foam with high electrical conductivity and large adsorption capability, *Appl. Surf. Sci.* 311 (2014) 808–815.

[24] Y. Zhu, S. Murali, M.D. Stoller, K.J. Ganesh, W. Cai, P.J. Ferreira, A. Pirkle, R.M. Wallace, K.A. Cybrosz, M. Thommes, Carbon-based supercapacitors produced by activation of graphene, *Science* 332 (2011) 1537.

[25] X.C. Dong, H. Xu, X.W. Wang, Y.X. Huang, M.B. Chan-Park, H. Zhang, L.H. Wang, W. Huang, P. Chen, 3D graphene-cobalt oxide electrode for high-performance supercapacitor and enzymeless glucose detection, *ACS Nano* 6 (2012) 3206.

[26] Z. Niu, J. Chen, Huey H. Hng, J. Ma, X. Chen, A leavening strategy to prepare reduced graphene oxide foams, *Adv. Mater.* 24 (2012) 4144–4150.

[27] E. Singh, Z. Chen, F. Houshamd, W. Ren, Y. Peles, H.M. Cheng, N. Koratkar, Superhydrophobic graphene foams, *Small* 9 (2013) 75–80.

[28] Y. Xu, K. Sheng, C. Li, G. Shi, Self-assembled graphene hydrogel via a one-step hydrothermal process, *ACS Nano* 4 (2010) 4324–4330.

[29] B. Qiu, M. Xing, J. Zhang, Mesoporous TiO<sub>2</sub> nanocrystals grown in situ on graphene aerogels for high photocatalysis and lithium-ion batteries, *J. Am. Chem. Soc.* 136 (2014) 5852.

[30] T. Xia, M. Kovochich, M. Liou, L. Madler, B. Gilbert, H.B. Shi, J.I. Yeh, J.I. Zink, A.E. Nel, Comparison of the mechanism of toxicity of zinc oxide and cerium oxide nanoparticles based on dissolution and oxidative stress properties, *ACS Nano* 2 (2008) 2121–2134.

[31] M. Auffan, J. Rose, M.R. Wiesner, J.Y. Bottero, Chemical stability of metallic nanoparticles: a parameter controlling their potential cellular toxicity in vitro, *Environ. Pollut.* 157 (2009) 1127–1133.

[32] J.Q. Tian, R. Ning, Q. Liu, A.M. Asiri, A.O. Al-Youbi, X.P. Sun, Three-dimensional porous supramolecular architecture from ultrathin g-C<sub>3</sub>N<sub>4</sub> nanosheets and reduced graphene oxide: solution self-assembly construction and application as a highly efficient metal-free electrocatalyst for oxygen reduction reaction, *ACS Appl. Mater. Interface* 6 (2014) 1011–1017.

[33] H. Hu, Z.B. Zhao, Q. Zhou, Y. Gogotsi, J.S. Qiu, The role of microwave absorption on formation of graphene from graphite oxide, *Carbon* 50 (2012) 3267–3273.

[34] S. Martha, A. Nashim, K.M. Parida, Facile synthesis of highly active g-C<sub>3</sub>N<sub>4</sub> for efficient hydrogen production under visible light, *J. Mater. Chem. A* 1 (2013) 7816–7824.

[35] L. Liu, Y.H. Qi, J.R. Lu, S.L. Lin, W.J. An, Y.H. Liang, W.Q. Cui, A stable Ag<sub>3</sub>PO<sub>4</sub>@g-C<sub>3</sub>N<sub>4</sub> hybrid core@shell composite with enhanced visible light photocatalytic degradation, *Appl. Catal. B-Environ.* 183 (2016) 133–141.

[36] X.C. Wang, S. Blechert, M. Antonietti, Polymeric graphitic carbon nitride for heterogeneous photocatalysis, *ACS Catal.* 2 (2012) 1596–1606.

[37] S. Fujita, H. Habuchi, S. Takagi, H. Takikawa, Optical properties of graphitic carbon nitride films prepared by evaporation, *Diam. Relat. Mater.* 65 (2016) 83–86.

[38] J. Lu, Y. Wang, J.F. Huang, L.Y. Cao, J.Y. Li, G.J. Hai, Z. Bai, One-step synthesis of g-C<sub>3</sub>N<sub>4</sub> hierarchical porous structure nanosheets with dramatic ultraviolet light photocatalytic activity, *Mater. Sci. Eng. B-Adv.* 214 (2016) 19–25.

[39] Y.B. Li, H.M. Zhang, P.R. Liu, D. Wang, Y. Li, H.J. Zhao, Cross-linked g-C<sub>3</sub>N<sub>4</sub>/rGO nanocomposites with tunable band structure and enhanced visible light photocatalytic activity, *Small* 9 (2013) 3336–3344.

[40] H. Hu, Z.B. Zhao, W.B. Wan, Y. Gogotsi, J.S. Qiu, Ultralight and highly compressible graphene aerogels, *Adv. Mater.* 25 (2013) 2219–2223.

[41] K. Bindumadhan, S.K. Srivastava, S. Mahanty, MoS<sub>2</sub>-MWCNT hybrids as a superior anode in lithium-ion batteries, *Chem. Commun.* 49 (2013) 1823–1825.

[42] G.Q. Wang, J. Zhang, S. Kuang, W. Zhang, Enhanced electrocatalytic performance of a porous g-C<sub>3</sub>N<sub>4</sub>/graphene composite as a counter electrode for dye-sensitized solar cells, *Chem.-Eur. J.* 22 (2016) 11763–11769.

[43] J. Yu, Y.P. Liu, X.H. Liu, C.P. Wang, J.F. Wang, F.X. Chu, C.B. Tang, Integration of renewable cellulose and rosin towards sustainable copolymers by grafting from ATRP, *Green Chem.* 16 (2014) 1854–1864.

[44] H.Y. Liu, T. Kuila, N.H. Kim, B.C. Ku, J.H. Lee, In situ synthesis of the reduced graphene oxide-polyethylenimine composite and its gas barrier properties, *J. Mater. Chem. A* 1 (2013) 3739–3746.

[45] H.Y. Na, L. Zhang, H.X. Qiu, T. Wu, M.X. Chen, N. Yang, L.Z. Li, F.B. Xing, J.P. Gao, A two step method to synthesize palladium-copper nanoparticles on reduced graphene oxide and their extremely high electrocatalytic activity for the electrooxidation of methanol and ethanol, *J. Power Sources* 288 (2015) 160–167.

[46] L.F. Lai, J.R. Potts, D. Zhan, L. Wang, C.K. Poh, C.H. Tang, H. Gong, Z.X. Shen, L.Y. Jianyi, R.S. Ruoff, Exploration of the active center structure of nitrogen-doped graphene-based catalysts for oxygen reduction reaction, *Energy Environ. Sci.* 5 (2012) 7936–7942.

[47] Y. Hou, Z.H. Wen, S.M. Cui, X.L. Feng, J.H. Chen, Strongly coupled ternary hybrid aerogels of N-deficient porous graphitic-C<sub>3</sub>N<sub>4</sub> nanosheets/N-doped graphene/NiFe-layered double hydroxide for solar-driven photoelectrochemical water oxidation, *Nano Lett.* 16 (2016) 2268–2277.

[48] J.J. Duan, S. Chen, M. Jaroniec, S.Z. Qiao, Porous C<sub>3</sub>N<sub>4</sub> nanolayers@N-graphene films as catalyst electrodes for highly efficient hydrogen evolution, *ACS Nano* 9 (2015) 931–940.

[49] W.C. Wan, S. Yu, F. Dong, Q. Zhang, Y. Zhou, Efficient C<sub>3</sub>N<sub>4</sub>/graphene oxide macroscopic aerogel visible-light photocatalyst, *J. Mater. Chem. A* 4 (2016) 7823–7829.

[50] K. Feng, B.B. Tang, P.Y. Wu, Sulfonated graphene oxide-silica for highly selective Nafton-based proton exchange membranes, *J. Mater. Chem. A* 2 (2014) 16083–16092.

[51] T.B. Limbu, F. Mendoza, D. Barriomuevo, J. Carpena, B. Maruyama, R.S. Katiyar, B.R. Weiner, G. Morell, Study on the optical and electrical properties of tetracyanoethylene doped bilayer graphene stack for transparent conducting electrodes, *AIPI Adv.* 6 (2016).

[52] X. Dai, M.L. Xie, S.G. Meng, X.L. Fu, S.F. Chen, Coupled systems for selective oxidation of aromatic alcohols to aldehydes and reduction of nitrobenzene into aniline using CdS/g-C<sub>3</sub>N<sub>4</sub> photocatalyst under visible light irradiation, *Appl. Catal. B-Environ.* 158 (2014) 382–390.

[53] Z.W. Tong, D. Yang, J.F. Shi, Y.H. Nan, Y.Y. Sun, Z.Y. Jiang, Three-dimensional porous aerogel constructed by g-C<sub>3</sub>N<sub>4</sub> and graphene oxide nanosheets with excellent visible-light photocatalytic performance, *ACS Appl. Mater. Interface* 7 (2015) 25693–25701.

[54] X.Q. Zhang, Z.G. Chi, B.J. Xu, C.J. Chen, X. Zhou, Y. Zhang, S.W. Liu, J.R. Xu, End-group effects of piezofluorochromic aggregation-induced enhanced emission compounds containing distyrylanthracene, *J. Mater. Chem.* 22 (2012) 18505–18513.

[55] B.Q. Peng, L. Chen, C.J. Que, K. Yang, F. Deng, X.Y. Deng, G.S. Shi, G. Xu, M.H. Wu, Adsorption of antibiotics on graphene and biochar in aqueous solutions induced by pi-pi interactions, *Sci. Rep.-UK* 6 (2016).

[56] C. Cui, Y.P. Wang, D.Y. Liang, W. Cui, H.H. Hu, B.Q. Lu, S. Xu, X.Y. Li, C. Wang, Y. Yang, Photo-assisted synthesis of Ag<sub>3</sub>PO<sub>4</sub>/reduced graphene oxide/Ag heterostructure photocatalyst with enhanced photocatalytic activity and stability under visible light, *Appl. Catal. B-Environ.* 158 (2014) 150–160.

[57] Y.J. Cui, Z.X. Ding, P. Liu, M. Antonietti, X.Z. Fu, X.C. Wang, Metal-free activation of H<sub>2</sub>O<sub>2</sub> by g-C<sub>3</sub>N<sub>4</sub> under visible light irradiation for the degradation of organic pollutants, *Phys. Chem. Chem. Phys.* 14 (2012) 1455–1462.

[58] J.F. Ma, K. Wang, L.Y. Li, T. Zhang, Y. Kong, S. Komarneni, Visible-light photocatalytic decolorization of orange II on Cu<sub>2</sub>O/ZnO nanocomposites, *Ceram. Int.* 41 (2015) 2050–2056.